

Accepted Manuscript

The role of ternary alloying elements in eutectoid transformation of U10Mo alloy part I. Microstructure evolution during arc melting and subsequent homogenization annealing in U9.8Mo0.2X alloy (X = Cr, Ni, Co)

Saumyadeep Jana, Lucas Sweet, Derek Neal, Alan Schemer-Kohn, Sean Agnew, Curt Lavender, Vineet Joshi

PII: S0022-3115(18)30382-9

DOI: [10.1016/j.jnucmat.2018.06.024](https://doi.org/10.1016/j.jnucmat.2018.06.024)

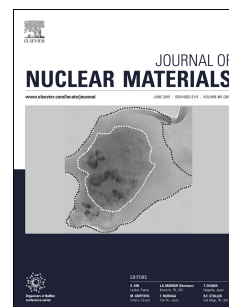
Reference: NUMA 51037

To appear in: *Journal of Nuclear Materials*

Received Date: 16 March 2018

Revised Date: 13 June 2018

Accepted Date: 14 June 2018



Please cite this article as: S. Jana, L. Sweet, D. Neal, A. Schemer-Kohn, S. Agnew, C. Lavender, V. Joshi, The role of ternary alloying elements in eutectoid transformation of U10Mo alloy part I. Microstructure evolution during arc melting and subsequent homogenization annealing in U9.8Mo0.2X alloy (X = Cr, Ni, Co), *Journal of Nuclear Materials* (2018), doi: 10.1016/j.jnucmat.2018.06.024.

This is a PDF file of an unedited manuscript that has been accepted for publication. As a service to our customers we are providing this early version of the manuscript. The manuscript will undergo copyediting, typesetting, and review of the resulting proof before it is published in its final form. Please note that during the production process errors may be discovered which could affect the content, and all legal disclaimers that apply to the journal pertain.

The role of ternary alloying elements in eutectoid transformation of U10Mo alloy

Part I. Microstructure evolution during arc melting and subsequent homogenization annealing in U9.8Mo0.2X alloy (X = Cr, Ni, Co)

Saamyadeep Jana^a, Lucas Sweet^a, Derek Neal^a, Alan Schemer-Kohn^a, Sean Agnew^b, Curt Lavender^a,
Vineet Joshi^a

^aPacific Northwest National Laboratory, PO Box 999, Richland, WA 99354

^bUniversity of Virginia-Arlington, 395 McCormick Road, Charlottesville, Virginia 22904

Abstract

This work describes the microstructural evolution in an alloy of uranium with 10 wt.% molybdenum (U10Mo), with minor addition of a third alloying element, namely, Cr, Ni, or Co, at 0.2 wt.%. The microstructures of arc-melted buttons in the as-cast condition show significant Mo segregation. The segregation behavior of Cr, Ni, and Co was investigated through detailed scanning electron microscope imaging. A homogenization heat treatment at 900 °C for 48 h results in uniform Mo distribution and associated grain growth in all of the four alloys that were fabricated. Further, formation of multiple phases was noted in U-9.8 wt.% Mo-0.2 wt.% Ni and U-9.8 wt.% Mo-0.2 wt.% Co alloys after the homogenization annealing step. The greatest grain-boundary-initiated eutectoid transformation as measured by % volume fraction was observed when the homogenized U-9.8 wt.% Mo-0.2 wt.% Ni alloy was aged at 500 °C for 20 h. The least eutectoid transformation occurred in U10Mo.

Keywords: UMo alloys, Phase transformation, Solidification, Heat treatment

1. Introduction

Development of uranium-molybdenum metallic alloy fuel has been the primary focus of the U.S. Department of Energy National Nuclear Security Administration's Office of Conversion within the Office of Material Minimization and Management (M3), to support the conversion of research reactors and radioisotope production facilities to use of low-enriched uranium (LEU, ≤ 20 wt.% of the fissile uranium isotope ^{235}U) fuel instead of highly enriched uranium fuel [1-4] (HEU, > 20 wt.% of the fissile uranium isotope ^{235}U , often ≥ 90 wt.%). The use of a low enriched uranium core requires a direct increase either in the fuel loading or in the total density of uranium atoms in the fuel to keep the neutronics unaffected [1, 5]. This has prompted development of uranium monolithic fuel foils with the highest possible uranium density in the fuel region. Pure metallic uranium cannot be used as a nuclear fuel because it has

unfavorable burnup characteristics (cavitation swelling under irradiation and thermal and irradiation growth under power ramping) in its room-temperature orthorhombic crystal structure (α -U) [6]. However, the high-temperature body-centered cubic (BCC) γ -U phase has adequate properties (stable behavior under low-burnup, high temperature irradiation conditions on account of swelling through fission gas nucleation and growth) for use as a nuclear fuel [3]. Alloying addition can stabilize the γ -U phase at room temperature, and, among several possible U alloys, UMo alloys provide higher uranium density and γ stability, and possesses acceptable irradiation stability, mechanical properties, corrosion resistance and is formed over a wide range of Mo concentration [3, 4, 7-9]. Further, Mo has a lower parasitic absorption cross-section for neutrons [10]. Foils consisting of U–10 wt.% Mo (U10Mo) have been chosen for converting the remaining high power research reactors operating with HEU. Densities of up to 8 g and 17 g U cm⁻³ can be achieved with U-Mo as dispersion fuel (in Al matrix) and as monolithic fuel, respectively [11, 12].

According to the equilibrium phase diagram of the UMo system shown in Fig. 1, the high-temperature γ -UMo phase (space group *Im3m*) decomposes into orthorhombic α -U (space group *Cmcm*) and body-centered tetragonal γ' -phase (U₂Mo, space group *I4/mmm*) through a eutectoid transformation below the eutectoid temperature $\sim 560^\circ$ C. There is some uncertainty in the measurement of the precise composition and temperature of the eutectoid transformation in U-Mo system, for example, $565^\circ\text{C} \pm 5$ for U-10.5 wt.% Mo [13], 560°C for U-10 wt.% Mo [14], 556°C for U-9.7 wt.% Mo [15], and 555°C for U-11.1 wt.% Mo [16]. The eutectoid reaction in the UMo system initiates through a discontinuous precipitation (DP) or cellular reaction mechanism, which results in the formation of α -U + Mo-rich γ -UMo lamellar microstructure mostly along the prior γ -UMo grain boundaries [17-23]. In our recent study [17, 18], we have observed evidence of DP reaction initiation within one hour of exposure at 500°C , leading to α -U lamellar structure formation, which is undesirable for in-reactor operations. In more recent studies, we observed that the presence/location of impurity elements were responsible for acceleration or retardation of the kinetics of the DP phase transformation [24]. In earlier studies, it was observed that the feedstock materials used to fabricate these fuel plates contain impurities up to 2000 ppm. The two major impurity elements were C and Si, each having greater than 300 ppm concentrations. Fe, K, P, S, Na, Mg, Al, Ca, B, Ni, and Mn occurred in concentrations greater than 30 ppm [24]. The effect of these impurities on the phase transformation kinetics is not well understood and has not been documented well.

DP is a well known phenomenon in various alloy systems. For example, AZ91, one of the most widely used Mg-alloy, containing 9 wt.% Al, 0.8 wt.% Zn, and 0.2 wt.% Mn, exhibits DP at elevated temperatures ($> 120^{\circ}\text{C}$), leading to formation of a lamellar combination of $\text{Mg}_{17}\text{Al}_{12}$ and Al enriched α -Mg phases at the grain boundaries, and, thus show poor creep properties [25]. Literature data shows that the addition of certain alloying elements such as Ca, Sr and rare earth elements into AZ91 can improve its high temperature strength and creep properties, by reducing the amount of $\text{Mg}_{17}\text{Al}_{12}$ phase through suppression of the discontinuous precipitation of $\text{Mg}_{17}\text{Al}_{12}$ phase and the formation of alternative, thermally stable, intermetallic compounds at grain boundaries [26-29]. Therefore, in a similar fashion, it may be possible to alter the nature of DP reaction in UMo system through minor addition of a ternary alloying element. Previously, Repas et al. [19] investigated the effect of minor Ti addition in the transformation characteristics of U8Mo system. It was found that Ti additions up to 1 wt.% result in a very slight increase in the rate of DP reaction kinetics. The most significant effect of Ti addition on the transformation characteristics of the U8Mo alloy was the appearance of a new reaction, precipitation of the ϵ -phase (bcc solid solution of Mo and Ti, containing some U) in the high temperature range. Peterson [30] studied the effect of Zr addition in UMo system. It appears that Zr addition results in faster DP transformation kinetics due to ZrMo_2 formation.

In the current study, we examined the effects of minor additions of Cr, Ni, or Co on the DP transformation kinetics in U10Mo alloy. Hofman et al. [31] calculated the effectiveness of various transition metals as alloying elements for retaining γ -U phase in its metastable state upon cooling. In this study, a powerful stabilizing effect of a small addition of 4d transition metals with higher atomic numbers than Mo when added to U-Mo alloys has been noted. Addition of Zr and Nb decreases nucleation time relative to Mo, whereas Re, Ru, and Pt increase the nucleation time substantially. The powerful stabilizing effect of Pd and Pt (both having face-centered cubic (FCC) structure) was calculated experimentally. The other two elements that appear to be effective are Ru and Os, which have hexagonal close packed (HCP) crystal structure. Based on this observation, we investigated the phase stability of γ -U with addition of more common 3d transition elements: (i) Cr with BCC structure, (ii) Co with HCP structure, and (iii) Ni with FCC structure. The present work reports our initial findings on microstructure evolution of the various as-cast alloys, and the effect of subsequent homogenization annealing treatment.

2. Experimental Procedure

Four nominal U-Mo alloy compositions were studied in this work. These are (i) U-10 wt.% Mo (U10Mo), (ii) U-9.8 wt.% Mo-0.2 wt.% Cr (U9.8Mo0.2Cr), (iii) U-9.8 wt.% Mo-0.2 wt.% Co (U9.8Mo0.2Co), and (iv) U-9.8 wt.% Mo-0.2 wt.% Ni (U9.8Mo0.2Ni). Alloy buttons were fabricated in a Buehler Mini-Arc Melting Main Unit, which consists of a tungsten electrode and a water-cooled cold copper crucible housed inside a cylindrical vacuum chamber. Temperature measurement of the copper hearth during melting was not attempted. Depleted uranium (DU) alloyed with 9 wt.% Mo was used as the source of uranium. It was subsequently alloyed with Mo (99.97% purity), Cr, Ni (99.98% purity), and Co (99.998% purity) to achieve the target alloy compositions. A vacuum level of $5.0\text{--}8.0 \times 10^{-4}$ mbar, followed by backfilling with Ar to 0.3–0.7 bar was maintained during the arc-melting procedure. Zr was used as a getter. Each button was melted at least four times to promote compositional homogeneity. Separate chemical analysis on the as-cast buttons was not done.

Following arc melting, sections from each of the four as-cast buttons were subjected to a homogenization heat treatment to achieve compositional uniformity. The homogenization heat treatment was done inside an Ar-atmosphere furnace to suppress uranium oxidation. Individual samples were wrapped in Zr foil for further protection from oxidation. All the sections were homogenized at 900 °C for 48 h, followed by furnace cooling [32, 33]. Additionally, one section each from the U9.8Mo0.2Co and U9.8Mo0.2Ni buttons were homogenized at 830 °C and 790 °C for 48 h, respectively, with subsequent furnace cooling. The heating rate and the cooling rate during the homogenization treatment were determined to be 10 °C/min and 2 °C/min respectively. Once the furnace controller reached the desired temperature, the heat-treatment time began. After the specified duration, the samples were furnace cooled to room temperature.

Following heat treatment, individual samples were mounted, ground, and polished to 0.05 µm finish using a standard metallographic procedure [34]. Microstructure examinations of the various U-Mo arc-melted samples were conducted on a JEOL JSM-7600F scanning electron microscope (SEM) using the Low-Angle Backscattered Electron Detector (LABe) for imaging. Image collection used a 30 keV electron beam with an approximate probe current of 6 nA and a working distance of 8 mm from the objective lens. Energy-dispersive x-ray spectroscopy (EDS) data was collected on the Oxford X-Max 80 mm² silicon drift energy-dispersive x-ray detector and analyzed with the Oxford AZtec Nanoanalysis Suite version 3.2

SP1. Compositional data collection used a 10 keV electron beam, an approximate probe current of 10 nA and a working distance of 15 mm. The probe current setting was chosen to give a detector dead time of approximately 45%. EDS work was carried out separately at a lower kV in an effort to have better spatial resolution for composition analysis.

X-ray diffraction (XRD) data was collected on these four alloys using a Rigaku Ultima IV powder x-ray diffractometer equipped with a Cu x-ray tube operating at 40 kV and 40 mA, a vertical θ/θ goniometer with a 285 mm radius, and a D/teX linear position-sensitive silicon strip detector. A Ni filter was used to reduce the contribution of $K\beta$ x-rays. An Eulerian cradle with automated sample height adjustment and sample rotation was used. Full pattern Rietveld refinement was performed using the TOPAS V5 software package (Bruker). Fundamental parameter type peak shapes were used in the refinement. The instrument contribution to peak broadening was determined by fitting three functions—a Lorentzian function with $1/\cos(\theta)$ dependence, a hat function, and a circles function with $1/\tan(\theta)$ dependence—to a diffraction pattern of National Institute of Standards and Technology Standard Reference Material (NIST SRM) 640d collected using the same slit settings as this sample. The instrument zero error was also determined using the NIST SRM 640d. A first-order Chebyshev polynomial with a $1/x$ function was used to model the background.

3. Results and Discussion

3.1. Microstructure of the as-cast buttons

The microstructure of the U10Mo as-cast button is shown in Fig. 2. A lower magnification image, shown in Fig. 2a, clearly shows presence of dendritic microstructure in the U10Mo alloy. Solidification in the U-Mo binary system initiates with the first crystals that form containing significantly higher Mo content than the average composition (see UMo binary phase diagram, Fig. 1), resembling a cored microstructure. The centers of the dendrites remain rich in Mo, and hence show darker contrast in backscattered electron (BSE) imaging mode (due to lower atomic number), and the interdendritic regions show brighter contrast due to lower Mo, and therefore higher U, content. In a recent study, Pedrosa et al. [35] depicts in detail the solidification microstructure and related Mo segregation in alloys of U with 5–12 wt.% Mo. Similar microstructure was observed by Joshi et al. [32, 36] when they used pin-cast samples for compression testing. Similarly, the presence of Mo segregation is confirmed in the current study, although the rate of cooling is anticipated to be much faster than the cooling rate, which

is reported to be 30° C/min between 600-300° C interval, experienced during ingot melting method used by Pedrosa et al. [35], Although, we were not able to determine the cooling rate during solidification of the arc-melted buttons, the microstructural examination reveals the secondary dendrite arm spacing (SDAS) to be ~10 µm. Such a small SDAS value is a result of a faster cooling rate associated with the arc-melting procedure. In the case of Pedrosa et al.'s work, the SDAS is estimated to be ~ 100 µm in the as-cast U10Mo alloy. A closer look at Fig. 2a also reveals presence of sharp, needle-like shapes, as shown by arrows. These sharp, needle-like features are predominantly present along low-Mo, high-U-containing interdendritic regions, as can be seen in a representative higher magnification image, Fig. 2b. In addition, there are comparatively larger dark, second-phase particles, which were determined to be U carbide (UC). It appears that the DU-9 wt.% Mo used as the source of uranium contains a small volume fraction (<1%) of UC, and hence all the alloys will contain a small amount of UC as a second phase.

Fig. 3a shows a low-magnification BSE-SEM image of the U9.8Mo0.2Cr alloy. Presence of a dendritic pattern, sharp, needle-like features along interdendritic regions, and second-phase UC particles is evident in the U9.8U0.2Cr alloy in as-cast condition. No other second-phase particles could be detected in the U9.8Mo0.2Cr sample. Micrographs of U9.8Mo0.2Cr looked very similar to U10Mo samples. The magnified image in Fig. 3b shows details of the sharp, needle-like features. It can be clearly seen that there is surface relief associated with these needle-like features (as shown by arrows). An electron shadow effect makes such surface relief appear dark during imaging. Additionally, these raised areas appear to maintain a certain orientation, which is possibly related to the underlying crystal orientation. According to earlier literature, diffusionless shear transformations can take place in U-Mo alloys under faster cooling conditions, especially when the Mo content is low (up to 12.5 at. %). A number of metastable phases can form as the high temperature γ -UMo phase is continuously cooled, e.g., γ^0 , γ_d^0 , α''_b , etc. [37-40]. In addition, impurity/alloying elements play a key role in determining the final microstructure. For example, Cr, which is a β -stabilizer [41], can promote shearing transformation in U alloys, and can lead to related martensitic phase. In the present study, observation of these raised areas along the interdendritic regions (high U and low Mo) under the condition of faster cooling, where solidification is taking place inside a water-cooled copper hearth, possibly indicates associated diffusionless transformations. Strain induced during solidification of the arc-melted buttons could be another possible reason for the formation of such features, as has been discussed in a recent study [42]. However, further high resolution imaging study is needed to correctly identify these phases.

Fig. 4a shows a low magnification BSE image of the U9.8Mo0.2Ni sample in as-cast condition. Fewer sharp, needle-like features are present than in U10Mo and U9.8Mo0.2Cr. Rather, a different phase having elongated morphology is seen along the interdendritic regions, which can be more clearly seen in the higher magnification images shown in Fig. 4b and 4c. Presence of UC and a lamellar structure typical of eutectic solidification is visible in Fig 4b. In Fig. 4c, a few surface relief marks (shown by arrows) were identified. However, the number density of the surface relief marks is significantly lower in comparison to U10Mo and U9.8Mo0.2Cr.

In Fig. 5a, a representative micrograph of U9.8Mo0.2Co in as-cast condition is shown. Similar to the U9.8Mo0.2Ni sample, the occurrence of the sharp, acicular features is significantly low. In addition, numerous second-phase particles are evident along interdendritic regions (marked by a double arrow), with a slightly brighter contrast than the UC particles. Additionally, eutectic-like structure exists at a few places in the U9.8Mo0.2Co sample (single arrow). Higher magnification images of the as-cast U9.8Mo0.2Co alloy are shown in Fig. 5b and 5c. A eutectic solidification structure along the interdendritic region is readily visible in Fig. 5b. Another type of second-phase particle present along the interdendritic region (marked as "Co-rich I") is shown in Fig. 5c. In the case of as-cast U9.8Mo0.2Co alloy, numerous Co-rich I type particles were identified along the interdendritic regions. In a few cases, these Co-rich I type particles lie adjacent to a UC particle (Fig. 5c). In comparison, the number density of eutectic solidification structures containing a type of particles marked "Co-rich II" was much smaller. No surface relief marks could be seen in the as-cast U9.8Mo0.2Co alloy. In summary, it appears that the microstructures of U10Mo alloy and U9.8Mo0.2Cr alloy are very similar, with no second-phase particles other than UC being present. Signs of extensive surface relief marks along the interdendritic regions, possibly the result of a diffusionless shear transformation, are present in both U10Mo and U9.8Mo0.2Cr. On the other hand, eutectic solidification microstructure and other second-phase particles apart from UC are noted in U9.8Mo0.2Ni and U9.8Mo0.2Co alloys. Further, the occurrence of surface relief marks is significantly lower in these two alloys.

EDS analysis was performed to investigate the degree of Mo segregation and other second-phase compositions in the various U-Mo alloys. The average Mo content in the U10Mo alloy was ~11 wt.%, which is significantly higher than our targeted value. It should be noted that EDS technique is not the best method for obtaining the actual composition, and a more rigorous alloy composition determination should be performed using other techniques. However, the EDS data can be used qualitatively to

understand the nature of alloying element segregation during solidification. EDS analysis of the U10Mo as-cast button, from the center of the dendrite and along the interdendritic region, shows the Mo contents to be ~13 wt.% and 9 wt.%, respectively, which explains the associated darker and brighter contrast difference in BSE-SEM images. EDS analysis of the U9.8Mo0.2Cr alloy in its as-cast state indicates typical Mo inhomogeneity. The centers of the dendrites were rich in Mo (~13 wt.%), and the interdendritic regions lean in Mo (~8 wt.%). Additionally, Cr segregated (~0.4 wt.%) towards interdendritic regions, i.e., low-Mo regions, with the centers of the dendrites essentially Cr-free. EDS analysis of the as-cast U9.8Mo0.2Ni button indicates Mo content of ~13 wt.% at the centers of dendrites, and 8% along the interdendritic regions. However, Ni was not detected at either location. A closer look at the as-cast U9.8Mo0.2Ni revealed that Ni is tied up in eutectic solidification microstructure (Fig. 4b), where the average Ni content was ~15 wt.%. EDS analysis of the as-cast U9.8Mo0.2Co sample indicates typical Mo segregation, with centers of the dendrites being rich in Mo (~13 wt.%), and interdendritic regions being lean in Mo (~8 wt.%). Further, two types of Co-rich second-phase particles were identified. As shown in Fig. 5c, Co-rich I type particles contained ~11 wt.% Co. As mentioned earlier, the as-cast microstructure contained numerous Co-rich I type particles, mostly along the interdendritic regions. Co content inside the darker phase (Co-rich II phase) of the eutectic structure (Fig. 5b) was ~24 wt.%. Additionally, Mo content around Co-rich phases was very low (~1–2 wt.%).

3.2. Microstructure of the buttons homogenized at 900 °C for 48 h

Fig. 6a shows a BSE-SEM image of the U10Mo alloy after homogenization annealing heat treatment of 48 h at 900 °C. The homogenization heat treatment results in uniform Mo distribution, and no Mo segregation is apparent based on SEM imaging. The Dendritic microstructure is completely absent. Second-phase UC particles are uniformly distributed, and appear to have spheroidized due to long-term annealing, in contrast with the as-cast state. The volume fraction of the second-phase UC particles was determined to be ~0.8 % using image analysis. In addition, the grain boundaries appear to be very clean, with occasional presence of a few UC particles. EDS analysis of the homogenized U10Mo alloy indicates Mo concentration to be uniform, ~11 wt.% across the sample. Significant grain growth has occurred due to long-term homogenization treatment.

Fig. 6b shows the microstructure of the U9.8Mo0.2Cr alloy after homogenization annealing treatment, which is very similar in appearance to the U10Mo alloy microstructure. Significant grain growth and removal of the dendritic structure have resulted from the homogenization heat treatment. The second-

phase UC particle volume fraction is estimated to be $\sim 0.8\%$, and no additional second phase particles could be observed. Further, the grain boundaries appear to be devoid of any second-phase precipitates. EDS analysis indicates a uniform Mo concentration of $\sim 10.5\text{ wt.}\%$. In as-cast condition, Cr remained segregated along the interdendritic regions. Homogenization treatment eliminated Cr segregation, and the Cr concentration within the grain interior is $\sim 0.2\text{ wt.}\%$.

Microstructure of the U9.8Mo0.2Ni alloy after homogenization annealing is shown in Fig. 7a. Compared to the as-cast condition, the dendritic microstructure is absent after the homogenization treatment, and significant grain growth has occurred. Homogenization heat treatment led to precipitation of a second phase with an elongated morphology (marked by single arrows) along the grain boundaries, which is clearly evident in Fig. 7b, captured at a higher magnification. Very fine precipitation can be also observed within the grain interior (marked by double arrows). However, the fine precipitation within the grain interior does not appear to be uniform. Rather, it appears to have a network-like structure. It should be noted that eutectic solidification microstructure was observed in as-cast U9.8Mo0.2Ni alloy (Fig. 4b). After homogenization treatment, such eutectic structure was not detected, and thus appears to have dissolved during the long-term annealing. The total volume fraction of the second phase particles is estimated to be $\sim 1\%$ in homogenized U9.8Mo0.2Ni alloy. The total volume fraction of the second phase made up of only UC in U10Mo and in U9.8Mo0.2Cr was 0.8% . The slightly higher volume fraction of second phase in U9.8Mo0.2Ni alloy may be associated with Ni-rich second phases. EDS analysis indicates the Ni content of the thin, elongated phases (shown by single arrows in Fig. 7b) present along the grain boundaries to be as high as $\sim 25\text{ wt.}\%$. EDS analysis on smaller precipitates (shown by double arrows in Fig. 7b) was not attempted because of the spatial resolution limit of EDS. In a few instances, the Ni-rich phase has been observed to lie adjacent to a UC particle. EDS analysis indicated no Ni within the grain interiors.

Microstructure of the U9.8Mo0.2Co alloy after homogenization annealing is shown in Fig. 8a. Absence of dendritic microstructure, uniform Mo distribution, and significant grain growth as a result of homogenization treatment are apparent in Fig. 8a. As mentioned earlier, U9.8Mo0.2Co in as-cast condition showed two types of Co-rich particles (Fig. 5). None of those Co-rich particles could be detected after homogenization treatment. Instead, there is formation of a necklace type of microstructure along the grain boundaries, as shown by arrows in Fig. 8a. Within the grain interior, spheroidized UC particles are distributed uniformly. The volume fraction of UC particles was estimated

to be 0.8 %, which agrees well with similar data obtained from homogenized U10Mo and U9.8Mo0.2Cr alloys. The volume fraction of grain boundary particles is estimated to be ~1 %. A higher magnification BSE-SEM image (Fig. 8b) from the grain boundary region provides more detail on the second-phase formation. A lamellar microstructure has formed along the grain boundary after homogenization annealing treatment in U9.8Mo0.2Co. The thin lamellar phase, shown by single arrows, shows significantly brighter contrast than the matrix, while the interlamellar region, shown by double arrows, shows slightly darker contrast than the matrix. Since the features are smaller than the spatial resolution limit of EDS, accurate estimation of the composition of such features is not possible through EDS. However, through EDS, we tried to obtain a qualitative idea of the composition. Based on the EDS analysis, Co is not present within the grain interior, i.e., in the matrix. The brighter, thin lamellar features were found to contain Co. The darker interlamellar regions were found to be richer in Mo (~13–14 wt.%) than the grain interior (~11 wt.%), and no Co could be detected. Based on the SEM images and the EDS analysis, it therefore appears that the Co-rich phases in as-cast state, either free-standing or tied up in a eutectic structure (Co-rich I and Co-rich II phases), dissolved during homogenization treatment. A new lamellar microstructure formed along the grain boundary comprising bright, Co-containing lamella and interlamellar regions enriched in Mo. It is not clear yet whether this reaction took place towards the latter half of the homogenization treatment or during slow furnace cooling, since the samples were not quenched. Given the bright appearance in BSE-SEM images of the thin Co-containing lamella, it is likely that these are U6Co compounds, and, therefore associated with a very high atomic number contrast.

Based on the EDS analysis, it therefore appears that only Cr remains in solid solution in U9.2Mo0.2Cr after homogenization, and no Cr-rich phases form. However, neither Ni nor Co could be dissolved during homogenization. Presence of Ni-rich and Co-rich phases was detected after homogenization treatment at 900 °C for 48 h in U9.8Mo0.2Ni and U9.8Mo0.2Co, respectively. In an effort to check whether homogenization heat-treatment temperature affects Ni/Co dissolution behavior, two more heat-treatment studies were carried out. One as-cast section from the U9.8Mo0.2Ni alloy was heat treated at 790 °C for 48 h followed by furnace cooling. The microstructure is shown in Fig. 9. The BSE-SEM image captured at a lower magnification (Fig. 9a) shows that Mo homogenization is not complete, and there are signs of remnant dendritic pattern. UC particles do not appear to have spheroidized, and therefore have higher number density than after homogenization at 900 °C. A higher magnification image (Fig. 9b) from the same sample shows a long, Ni-rich phase along the grain boundary, together with finer precipitates inside the grain interior, and is very similar in appearance to Fig. 7b. No Ni was detected in

the grain interior matrix through EDS analysis. For the as-cast U9.8Mo0.2Co alloy, a different homogenization at 830 °C for 48 h was attempted. The microstructure, which is shown in Fig. 10a, shows no evidence of a visible dendritic pattern. At a higher magnification, formation of a lamellar microstructure along the grain boundary is clearly visible (Fig. 10b), which is similar in appearance to that observed after homogenization heat treatment of U9.8Mo0.2Co at 900 °C for 48 h (Fig. 8b). EDS analysis detected no Co in the grain interior.

To determine the effect of alloying element addition on the eutectoid transformation kinetics, one subeutectoid heat-treatment experiment was carried out. One piece each from U10Mo, U9.8Mo0.2Cr, U9.8Mo0.2Ni, and U9.8Mo0.2Co was first homogenized at 900 °C for 48 h, followed by furnace cooling. Afterwards, the homogenized samples were heat treated at 500 °C for 20 h, and subsequently furnace cooled, to initiate the eutectoid transformation. The microstructure after 500 °C/20 h heat treatment is summarized in a set of low magnification optical micrographs (Fig. 11). The amount of eutectoid transformation that initiates on grain boundaries through DP mechanism is very small in U10Mo (Fig. 11a) and U9.8Mo0.2Cr (Fig. 11b). However, the U9.8Mo0.2Ni alloy shows a significantly higher volume fraction of DP-based eutectoid transformation (Fig. 11c). The volume fraction of DP-based eutectoid transformation in U9.8Mo0.2Co seems to be intermediate (Fig. 11d). In addition, some finer network-like microstructural features that remain optically unresolved could be seen within the γ -UMo grain interior in heat-treated U9.8Mo0.2Co alloy. The transformed volume fractions measured through image analysis technique were 0.8%, 1.6%, 15.3%, and 3% in U10Mo, U9.8Mo0.2Cr, U9.8Mo0.2Ni, and U9.8Mo0.2Co alloys, respectively. It was also noted that there is less γ -UMo grain growth during 900 °C homogenization annealing in either of the three U9.8Mo0.2X (X = Cr, Ni, Co) alloys than in U10Mo.

In order to better understand the morphology of the eutectoid transformation products in all four alloys, BSE-SEM images at a higher magnification were captured, as shown in Fig. 12. Eutectoid transformation through DP initiates along the prior γ -UMo grain boundary; one such transformation region for the U10Mo alloy is shown in Fig 12a, where the lamellar nature of the reaction is evident, as reported in our previous studies [17, 18]. In the case of U9.8Mo0.2Cr, the lamellar morphology of the DP transformation products is very similar in appearance to that observed in U10Mo (Fig. 12b). In both these alloys, the γ -UMo grain interior appears to be featureless. In U9.8Mo0.2Ni, the DP transformation product volume fraction is the highest. Significant growth of the DP reaction front into the prior γ -UMo grain interior has occurred. One such transformation region is shown in Fig. 12c. Apart from the typical

long, thin, dark lamellae, which are also present in U10Mo and U9.8Mo0.2Cr, presence of brighter contrast, short lamellae (shown by an arrow) is noted. Higher resolution imaging is needed to obtain structure/composition information about these short, bright phases. Fig. 12d shows the microstructure of the transformed region in U9.8Mo0.2Co alloy. A lamellar microstructure consisting of thin, bright lamella can be seen along the grain boundary (marked by a single long, black arrow). This structure corresponds to that observed after homogenization treatment of U9.8Mo0.2Co at 900 °C or 830 °C (Fig. 8b, 10b). Subsequently, there is formation of the typical lamellar microstructure associated with eutectoid transformation in the UMo alloy system, which is made up of thin, dark lamella (marked by a short, double, black arrow). There is also a uniform precipitation of interpenetrant dark, needle-like structure (marked by a long, double, black arrow), and a necklace-like structure (marked by long, red arrows) within the γ -UMo grain interior.

3.3. XRD phase analysis

XRD analysis was carried out to learn about the phase evolution during homogenization and subsequent subeutectoid annealing treatment. XRD profiles of all four alloys are represented in Fig. 13a-d. The XRD data has been presented in log-scale for easier comparison purpose. The collected XRD data for all four alloys indicated they have larger grain sizes than can be measured with the diffractometer used (>200 nm). For all of the alloys, the relative intensities of the peaks did not match those expected for a random distribution of crystallites, which is a sign of preferred orientation. Arc melting and subsequent fast solidification in a water-cooled copper hearth can result in directional crystallite growth and related appearance of texture. The other possible reason for the peak-height mismatch could be the small number of crystallites being probed, because of the large crystallites and small sample size. Full pattern Rietveld refinement was used for phase identification.

Fig. 13a compares the XRD profiles of the U10Mo alloy after homogenization and after subsequent subeutectoid annealing treatment. BCC γ -UMo is the major phase, which has been indexed in Fig. 13a. In addition, a small amount of the common contaminant UC was identified (~1 wt.%). No other phase could be identified, which agrees well with our previous SEM observation that shows the smallest amount of eutectoid transformation among the four alloys occurs in U10Mo.

Fig. 13b summarizes the XRD profiles of U9.8Mo0.2Cr. BCC γ -UMo phase is the major phase in homogenized condition. After subeutectoid annealing, no phase other than the BCC γ -UMo phase was

identified except a small amount of UC (~1 wt.%). The sample appears to be heavily textured since the intensities do not match those of a random-crystallites collection.

XRD profiles of the U9.8Mo0.2Ni alloy are shown in Fig. 13c. BCC γ -UMo is the major phase in homogenized condition, and the sample shows signs of significant texture. After subeutectoid annealing, additional peaks emerge in U9.8Mo0.2Ni, although the intensities are weak. Careful Rietveld refinement indicates presence of U2Mo (13.5 wt.%), α -U (2.5 wt.%), and BCC γ -UMo (80 wt.%) in aged U9.8Mo0.2Ni. In addition, small peaks that correspond to U6Ni may also be present, based on the analysis. SEM images (Fig. 11c, 12c) indeed show significant phase transformation in U9.8Mo0.2Ni alloy after subeutectoid annealing.

Fig. 13d shows the XRD profiles of the U9.8Mo0.2Co alloy. After homogenization, BCC γ -UMo phase is the major phase in U9.8Mo0.2Co. SEM imaging of homogenized U9.8Mo0.2Co showed presence of a lamellar structure comprising thin, very bright lamella (Fig. 8b), which XRD phase analysis confirms to be U6Co. Additional peaks emerge in U9.8Mo0.2Co after subeutectoid annealing. Phase analysis indicates presence of U2Mo (19 wt.%), U6Co (4 wt.%), UC (1 wt.%), and the rest BCC γ -UMo. In Fig. 12d, a BSE-SEM image of U9.8Mo0.2Co alloy after subeutectoid annealing was shown. The micrograph clearly shows precipitation of a dark-contrast, needle-shaped phase with interpenetrant morphology inside the γ -UMo grain interior. That particular phase appears to be U2Mo based on XRD analysis, and must have formed through continuous precipitation (CP).

4. Conclusion

This work reports the evolution of microstructure in the UMo alloy system with minor addition of ternary alloying elements. The as-cast microstructure shows Mo segregation, with centers of the dendrites being rich in Mo in all four alloy systems. Some of the major findings of this study are summarized below:

- Addition of Cr in the UMo system leads to Cr segregation to Mo-lean, U-rich interdendritic regions, although no Cr-rich second phase is visible. Addition of Ni leads to formation of Ni-rich eutectic structure along interdendritic regions. Addition of Co leads to formation of two types of Co-rich phases along the interdendritic regions. Multiple surface relief marks were noticed in UMo and UMoCr alloys along U-rich interdendritic regions, which may be related to shear transformations.

- Homogenization treatment leads to removal of Mo segregation, and associated grain growth. EDS analysis indicates Cr dissolution in BCC γ -UMo matrix. However, Ni precipitates out along grain boundaries after homogenization treatment. In the UMoCo system, a network-like structure with lamellar morphology forms along the γ -UMo grain boundary after homogenization treatment.
- The degree of eutectoid transformation is the lowest in the UMo and UMoCr systems. The greatest amount of DP-based eutectoid transformation is observed in the UMoNi alloy. In the UMoCo alloy, considerable U₂Mo formation through CP occurs. Overall, it appears that eutectoid transformation in the U10Mo system is enhanced through addition of Ni or Co.
- The current study indicates the possibility of changing eutectoid transformation kinetics in UMo system through minor addition of 3d series transition elements.

Acknowledgements

This work was funded by the U.S. Department of Energy National Nuclear Security Administration's Office of Material Management and Minimization and performed at Pacific Northwest National Laboratory under contract DE-AC05-76RL01830.

References

- [1] J.L. Snelgrove, G.L. Hofman, M.K. Meyer, C.L. Trybus, T.C. Wiencek, Development of very-high-density low-enriched-uranium fuels, *Nuclear Engineering and Design* 178(1) (1997) 119-126.
- [2] D.E. Burkes, R. Prabhakaran, T. Hartmann, J.-F. Jue, F.J. Rice, Properties of DU-10 wt% Mo alloys subjected to various post-rolling heat treatments, *Nuclear Engineering and Design* 240(6) (2010) 1332-1339.
- [3] R.W. Cahn, P. Haasen, E.J. Kramer, B.R.T. Frost, *Materials Science and Technology: A Comprehensive Treatment. Nuclear materials*; volume editor, Brian R.T. Frost. Vol. 10A. Pt. I, VCH1994.
- [4] M.K. Meyer, J. Gan, J.F. Jue, D.D. Keiser, E. Perez, A. Robinson, D.M. Wachs, N. Woolstenhulme, G.L. Hofman, Y.S. Kim, Irradiation Performance of U-Mo Monolithic Fuel, *Nuclear Engineering and Technology* 46(2) (2014) 169-182.
- [5] Reduced Enrichment for Research and Test Reactors (RERTR), May 2009. <http://www.rertr.anl.gov>.
- [6] ASM International, *Properties and Selection: Non Ferrous Alloys and Special Purpose Materials*, 1990.
- [7] Development status of metallic, dispersion and non-oxide advanced and alternative fuels for power and research reactors, IAEA-TECDOC-1374, Vienna, 2003, p. 49.

- [8] K.H. Kim, D.B. Lee, C.K. Kim, G.E. Hofman, K.W. Paik, Characterization of U-2 wt% Mo and U-10 wt% Mo alloy powders prepared by centrifugal atomization, *J Nucl Mater* 245(2-3) (1997) 179-184.
- [9] V.P. Sinha, P.V. Hegde, G.J. Prasad, H.S. Kamath, Seventeenth Plansee Seminar, Reutte, Austria, 2009, pp. RM 78/1-16.
- [10] K. Kim, D.B. Lee, C.K. Kim, I.H. Kuk, K.W. Baek, Development of Uranium–Silicide and U–Mo alloy fuels by centrifugal atomization, *Studies on Fuels with Low Fission Gas Release*, Vienna, 1997, p. 77.
- [11] W. Petry, A. Rohrmoser, J.L. Falgoux, C. Jarousse, P. Boulcourt, A. Chabre, S. Dubois, P. Lemoine, S. Van den Berghe, A. Leenaers, IRIS-TUM Program on Full Size Plates-UMo Dispers, RRFM. www.rrfm2008.org, 2008.
- [12] A. Rohrmoser, W. Petry Reduced Enrichment Program for FRM II, Actual Status and a Principal Study of Monolithic Fuel for FRM II; RRFM. www.rrfm2006.org, 2006.
- [13] A.E. Dwight, The uranium-molybdenum equilibrium diagram below 900° C, *Journal of Nuclear Materials* 2(1) (1960) 81-87.
- [14] T.B. Massalski, H. Okamoto, A.S.M. International, Binary alloy phase diagrams, ASM International, Materials Park, Ohio, 1990.
- [15] X. Zhang, Y.F. Cui, G.L. Xu, W.J. Zhu, H.S. Liu, B.Y. Yin, Z.P. Jin, Thermodynamic assessment of the U–Mo–Al system, *Journal of Nuclear Materials* 402(1) (2010) 15-24.
- [16] A. Berche, N. Dupin, C. Gueneau, C. Rado, B. Sundman, J.C. Dumas, Calphad thermodynamic description of some binary systems involving U, *J Nucl Mater* 411(1-3) (2011) 131-143.
- [17] S. Jana, A. Devaraj, L. Kovarik, B. Arey, L. Sweet, T. Varga, C. Lavender, V. Joshi, Kinetics of cellular transformation and competing precipitation mechanisms during sub-eutectoid annealing of U10Mo alloys, *Journal of Alloys and Compounds* 723 (2017) 757-771.
- [18] S. Jana, N. Overman, T. Varga, C. Lavender, V.V. Joshi, Phase transformation kinetics in rolled U-10 wt. % Mo foil: Effect of post-rolling heat treatment and prior gamma-UMo grain size, *Journal of Nuclear Materials* 496 (2017) 215-226.
- [19] P.E. Repas, Goodenow, R. H., Hehemann, R. F., Transformation Characteristics of U-Mo and U -Mo-Ti Alloys, *Transactions of American Society of Metals* 57 (1964) 150-163.
- [20] S. Neogy, M.T. Saify, S.K. Jha, D. Srivastava, G.K. Dey, Ageing characteristics of the metastable gamma phase in U–9 wt.% Mo alloy: experimental observations and thermodynamic validation, *Philosophical Magazine* 95(26) (2015) 2866-2884.
- [21] V.P. Sinha, P.V. Hegde, G.J. Prasad, G.K. Dey, H.S. Kamath, Phase transformation of metastable cubic γ -phase in U–Mo alloys, *Journal of Alloys and Compounds* 506(1) (2010) 253-262.

- [22] M.A. Steiner, C.A. Calhoun, R.W. Klein, K. An, E. Garlea, S.R. Agnew, alpha-Phase transformation kinetics of U-8 wt% Mo established by in situ neutron diffraction, *Journal of Nuclear Materials* 477 (2016) 149-156.
- [23] S. Saubert, R. Jungwirth, T. Zweifel, M. Hofmann, M. Hoelzel, W. Petry, Neutron and hard X-ray diffraction studies of the isothermal transformation kinetics in the research reactor fuel candidate U-8 wt% Mo, *Journal of Applied Crystallography* 49 (2016) 923-933.
- [24] Arun Devaraj, L. Kovarik, Elizabeth Kautz, Bruce Arey, Saumyadeep Jana, Curt Lavender, Vineet Joshi Grain boundary engineering to control the discontinuous precipitation in multicomponent U10Mo alloy, *Acta Materialia* 151 (2018) 181-190.
- [25] P. Zhang, Creep behavior of the die-cast Mg-Al alloy AS21, *Scripta Mater* 52(4) (2005) 277-282.
- [26] B. Nami, H. Razavi, S. Mirdamadi, S.G. Shabestari, S.M. Miresmaeili, Effect of Ca and Rare Earth Elements on Impression Creep Properties of AZ91 Magnesium Alloy, *Metall Mater Trans A* 41A(8) (2010) 1973-1982.
- [27] F. Khomamizadeh, B. Nami, S. Khoshkhouei, Effect of rare-earth element additions on high-temperature mechanical properties of AZ91 magnesium alloy, *Metall Mater Trans A* 36A(12) (2005) 3489-3494.
- [28] D. Amberger, P. Eisenlohr, M. Goken, Microstructural evolution during creep of Ca-containing AZ91, *Mat Sci Eng a-Struct* 510-11 (2009) 398-402.
- [29] K. Hirai, H. Somekawa, Y. Takigawa, K. Higashi, Effects of Ca and Sr addition on mechanical properties of a cast AZ91 magnesium alloy at room and elevated temperature, *Mat Sci Eng a-Struct* 403(1-2) (2005) 276-280.
- [30] C. A. W. Peterson, W.J.Steele, S. L. DiGiallonardo, Isothermal transformation study of some Uranium-base alloys, California University, Lawrence radiation Lab, Livermore, 1964.
- [31] G. L. Hofman, M.K.Meyer, A. E. Ray, DESIGN OF HIGH DENSITY GAMMA-PHASE URANIUM ALLOYS FOR LEU DISPERSION FUEL APPLICATIONS, The 1998 International Reduced Enrichment for Test Reactor Conference, Sao Paulo, Brazil, 1998.
- [32] V.V. Joshi, E.A. Nyberg, C.A. Lavender, D. Paxton, D.E. Burkes, Thermomechanical process optimization of U-10wt% Mo - Part 2: The effect of homogenization on the mechanical properties and microstructure, *J Nucl Mater* 465 (2015) 710-718.
- [33] Z.J. Xu, V. Joshi, S.Y. Hu, D. Paxton, C. Lavender, D. Burkes, Modeling the homogenization kinetics of as-cast U-10wt% Mo alloys, *J Nucl Mater* 471 (2016) 154-164.
- [34] V.J. Prabhakaran R, MA Rhodes, AL Schemer-Kohn, AD Guzman, and CA Lavender. , U 10Mo Sample Preparation and Examination using Optical and Scanning Electron Microscopy, Pacific Northwest National Laboratory, Richland, WA., 2016.

- [35] T.A. Pedrosa, A.M.M. dos Santos, F.S. Lameiras, P.R. Cetlin, W.B. Ferraz, Phase transitions during artificial ageing of segregated as-cast U-Mo alloys, *Journal of Nuclear Materials* 457 (2015) 100-117.
- [36] V.V. Joshi, E.A. Nyberg, C.A. Lavender, D. Paxton, H. Garmestani, D.E. Burkes, Thermomechanical process optimization of U-10 wt% Mo - Part 1: high-temperature compressive properties and microstructure, *J Nucl Mater* 465 (2015) 805-813.
- [37] J. Lehmann, R.F. Hills, Proposed Nomenclature for Phases in Uranium Alloys, *J Nucl Mater* 2(3) (1960) 261-268.
- [38] I. Tkach, N.T.H. Kim-Ngan, S. Maskova, M. Dzevenko, L. Havela, A. Warren, C. Stitt, T. Scott, Characterization of cubic gamma-phase uranium molybdenum alloys synthesized by ultrafast cooling, *Journal of Alloys and Compounds* 534 (2012) 101-109.
- [39] H.L. Yakel, A review of X-ray diffraction studies in uranium alloys, Vail, Colorado, 1974.
- [40] B.W. Howlett, A Study of Shear Transformations from Gamma-Phase in Uranium-Molybdenum Alloys Containing 6.0-12.5 at Percent Molybdenum, *J Nucl Mater* 35(3) (1970) 278-&.
- [41] V.K. Orlov, V.M. Teplinskaya, Structural features of martensite alpha-phases in alloys of uranium with transition metals, *Atomic Energy* 86(2) (1999) 118-125.
- [42] M.A. Steiner, E. Garlea, J. Creasy, A. DeMint, S.R. Agnew, Temperature dependent elastic properties of gamma-phase U-8 wt% Mo, *J Nucl Mater* 500 (2018) 184-191.

List of Figures

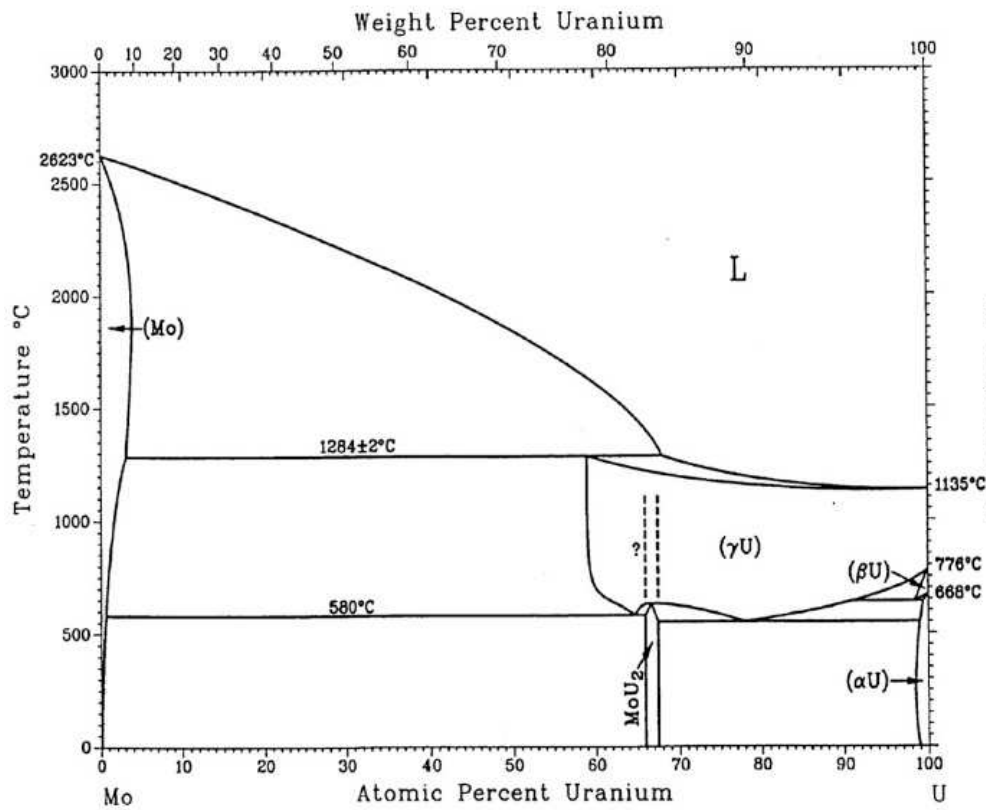


Fig. 1. U-Mo binary phase diagram [7].

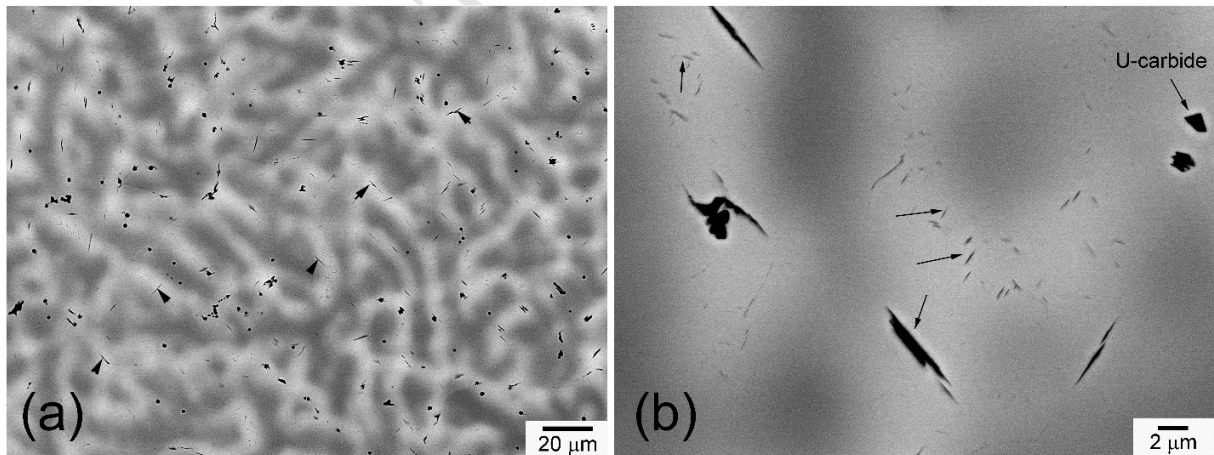


Fig. 2. As-cast U10Mo microstructure: (a) low-magnification image showing Mo segregation, (b) high-magnification image showing needle-like features present along interdendritic regions.

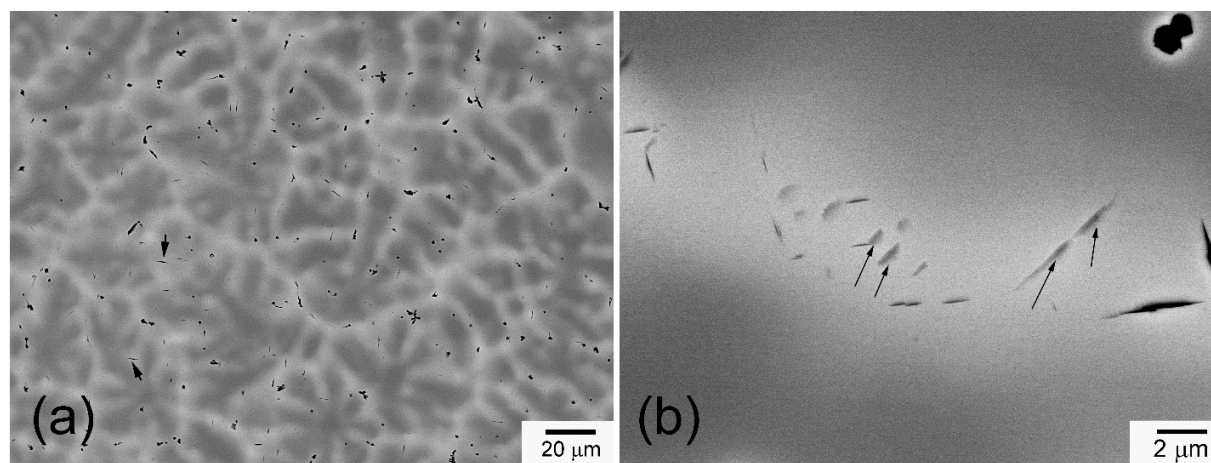


Fig. 3. As-cast U9.8Mo0.2Cr microstructure: (a) low-magnification image showing Mo segregation, (b) high-magnification image showing needle-like features to be surface relief marks.

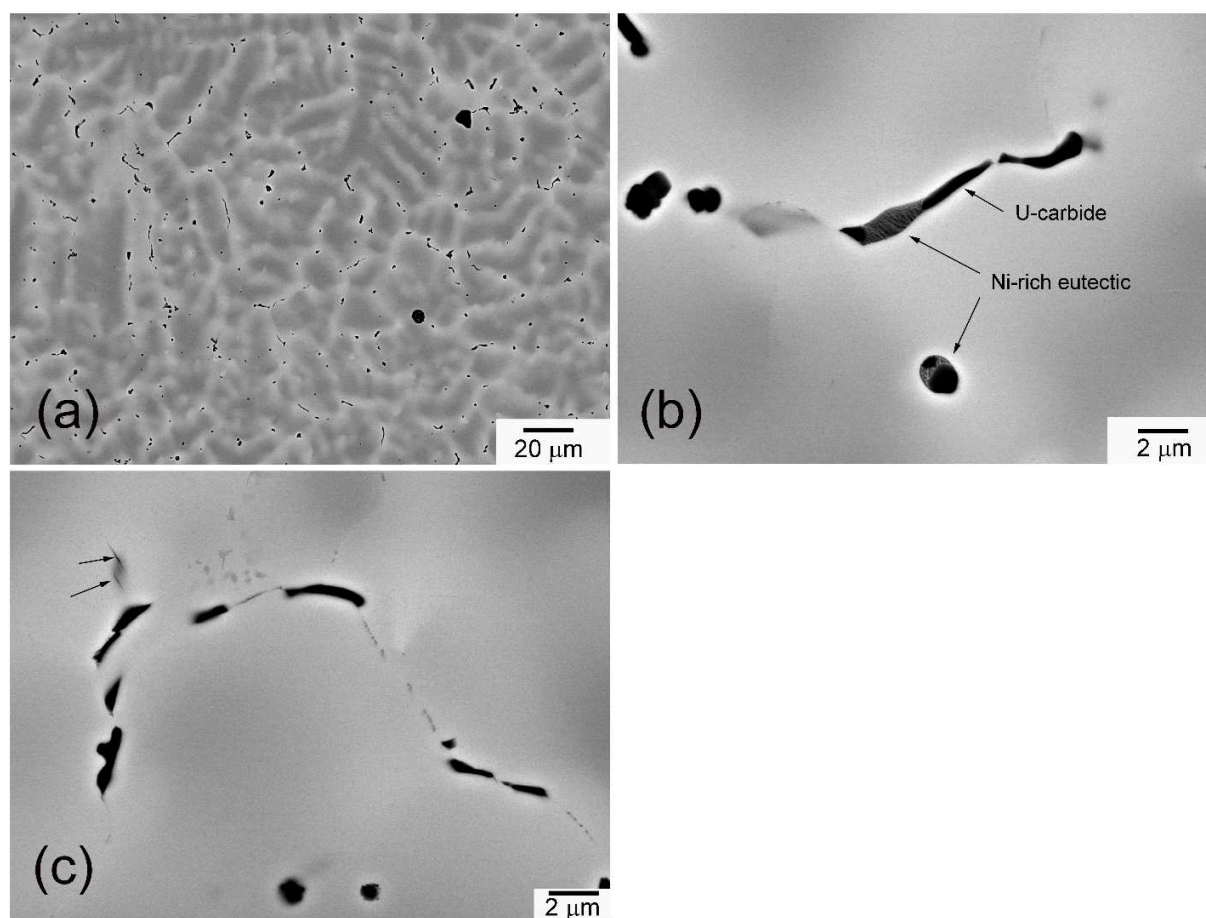


Fig. 4. As-cast UMoNi microstructure: (a) low-magnification, (b) Ni-rich eutectic present along interdendritic regions, (c) a few surface relief marks (shown by arrows) visible along Mo-lean and U-rich interdendritic regions.

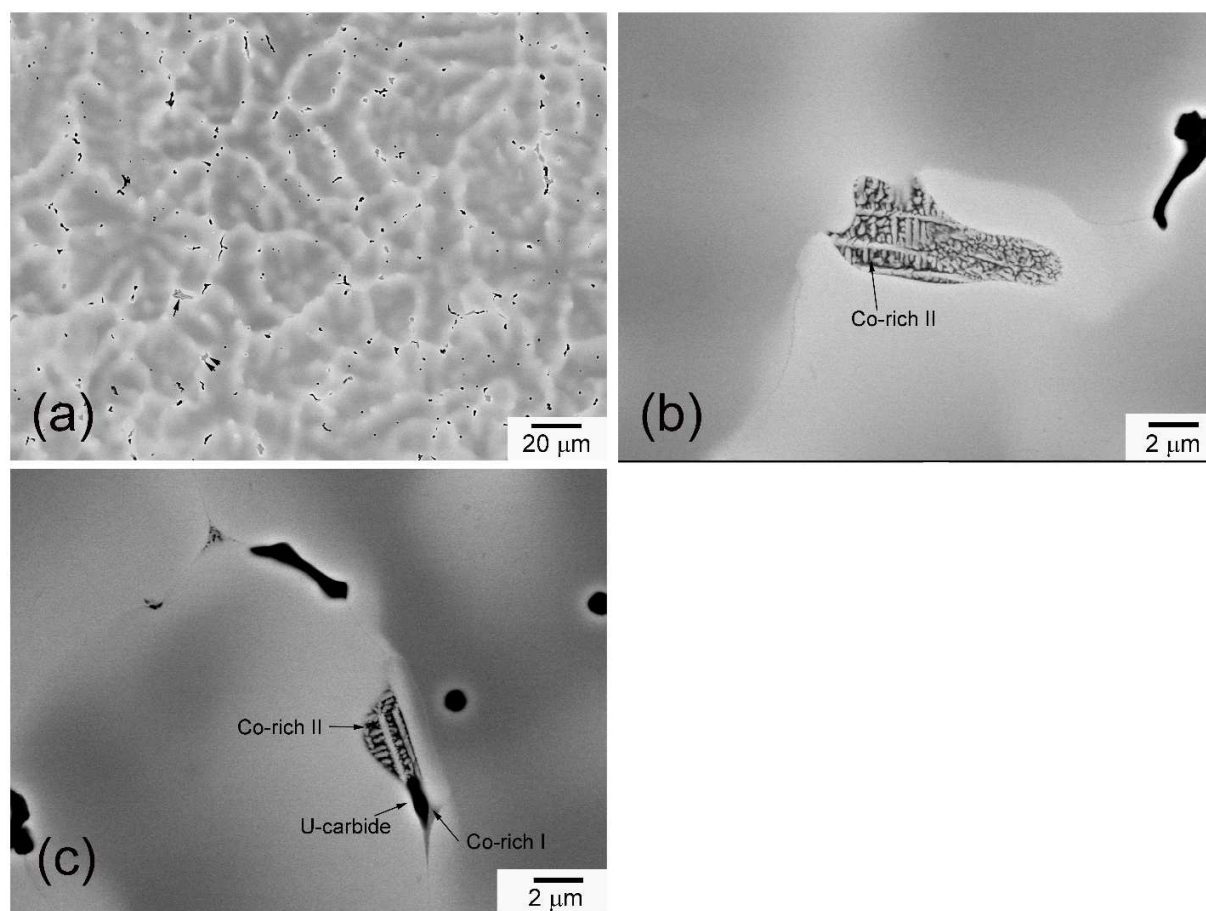


Fig. 5. As-cast UMoCo microstructure: (a) low-magnification, (b) Co-rich eutectic present along interdendritic regions, (c) two types of Co-rich phases (shown by arrows) present along Mo-lean and U-rich interdendritic regions.

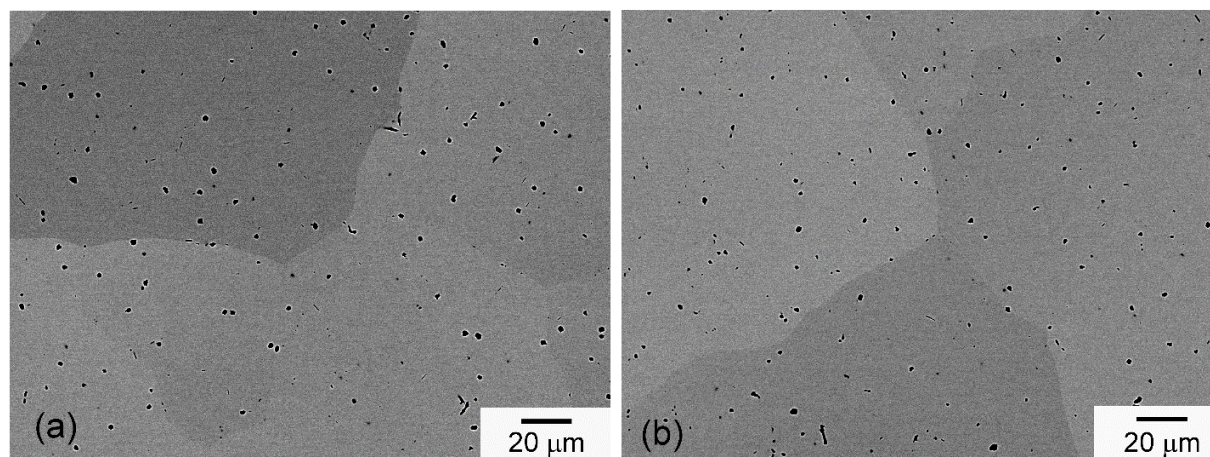


Fig. 6. Microstructure of the as-cast buttons after homogenization treatment at 900 °C for 48 h. (a) U10Mo, (b) U9.8Mo0.2Cr. Mo segregation is absent. No second phase other than UC is evident.

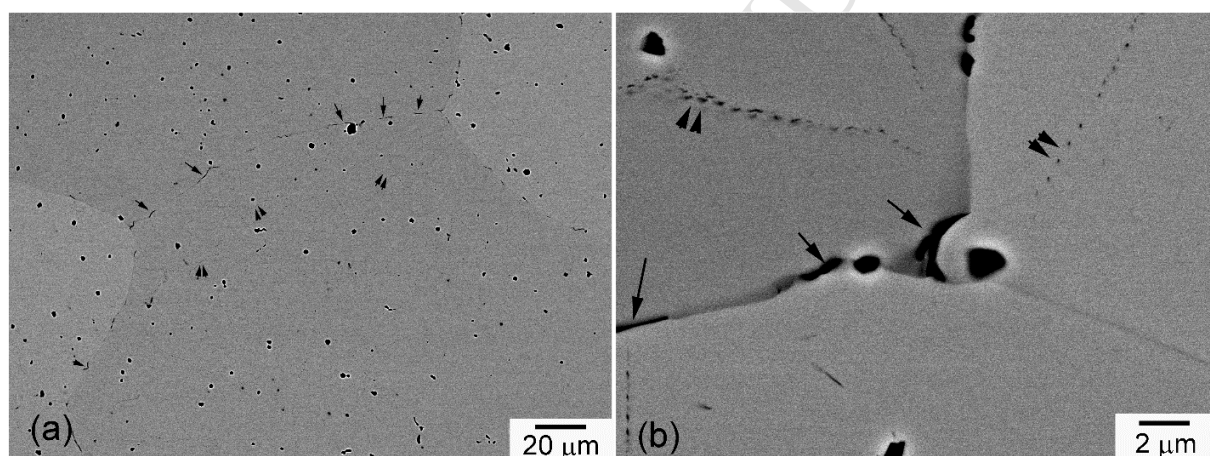


Fig. 7. BSE SEM image of the U9.8Mo0.2Ni alloy after homogenization treatment at 900 °C for 48 h. (a) Low-magnification image showing large grain structure due to heat treatment; (b) higher magnification image showing different precipitates. Single arrows show Ni-rich precipitates along grain boundaries, and double arrows show network-like precipitation within the grain interior.

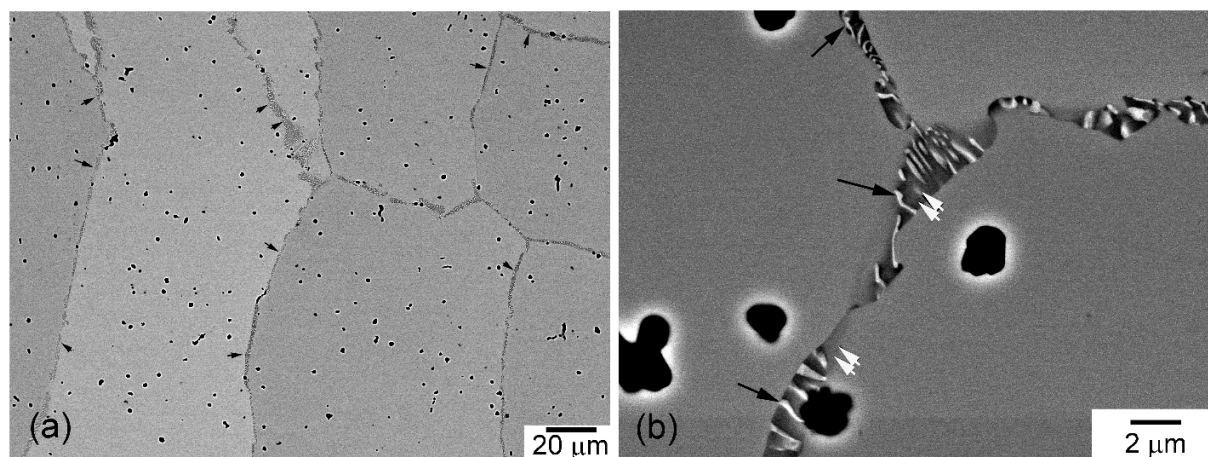


Fig. 8. Microstructure of the U9.8Mo0.2Co alloy after homogenization at 900 °C for 48 h. (a) low-magnification image showing necklace-type structure formation along grain boundary; (b) higher magnification image showing the lamellar structure associated with the necklace-type grain boundary phase.

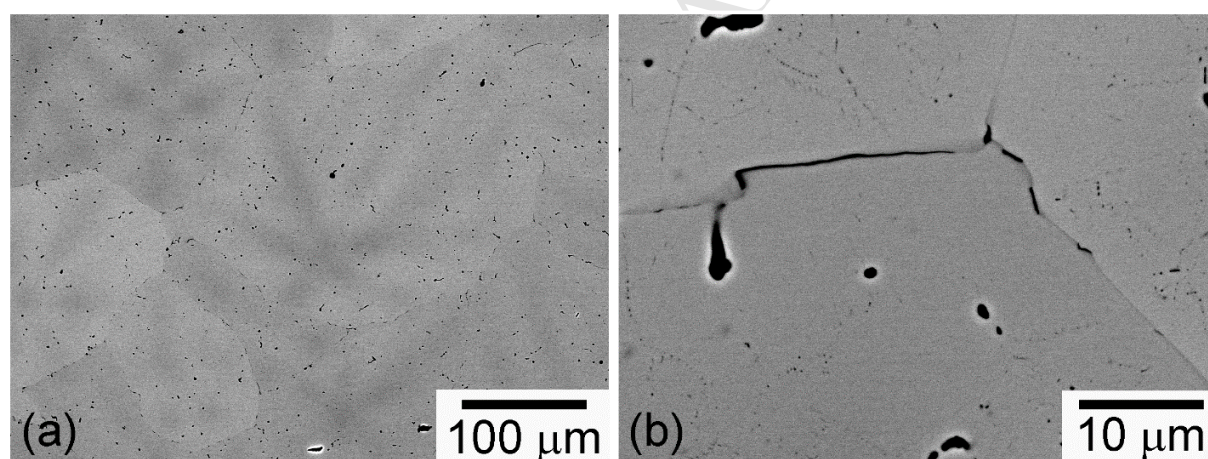


Fig. 9. U9.8Mo0.2Ni alloy after homogenization annealing at 790 °C for 48 h: (a) low-magnification image showing the remnant dendritic pattern; (b) higher magnification image showing precipitation of Ni-rich phase along the grain boundary, and nonuniform precipitation within the grain interior.

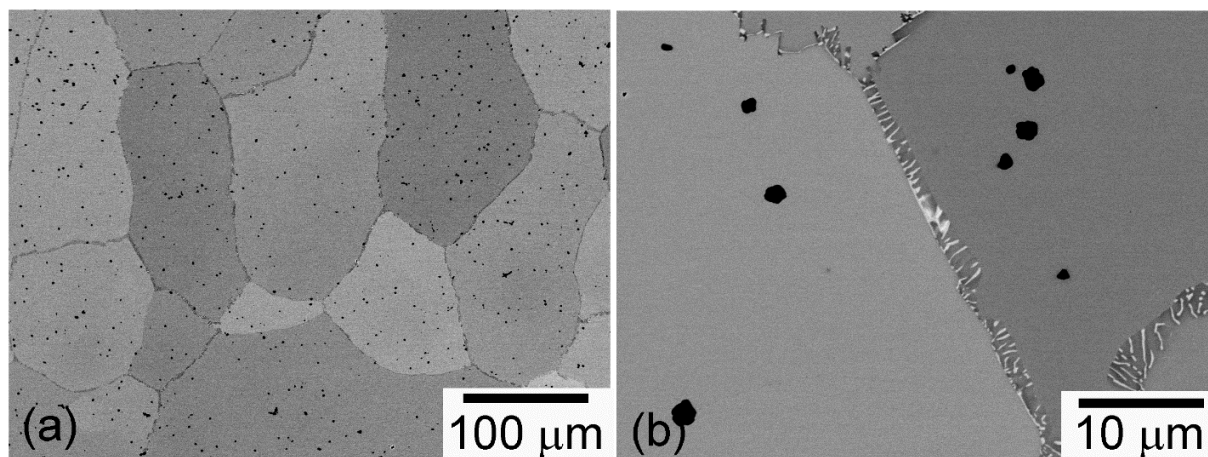


Fig. 10. U9.8Mo0.2Co alloy after homogenization annealing at 830 °C for 48 h: (a) low-magnification image; (b) higher magnification image showing precipitation of Co-rich phase in a lamellar morphology along grain boundaries.

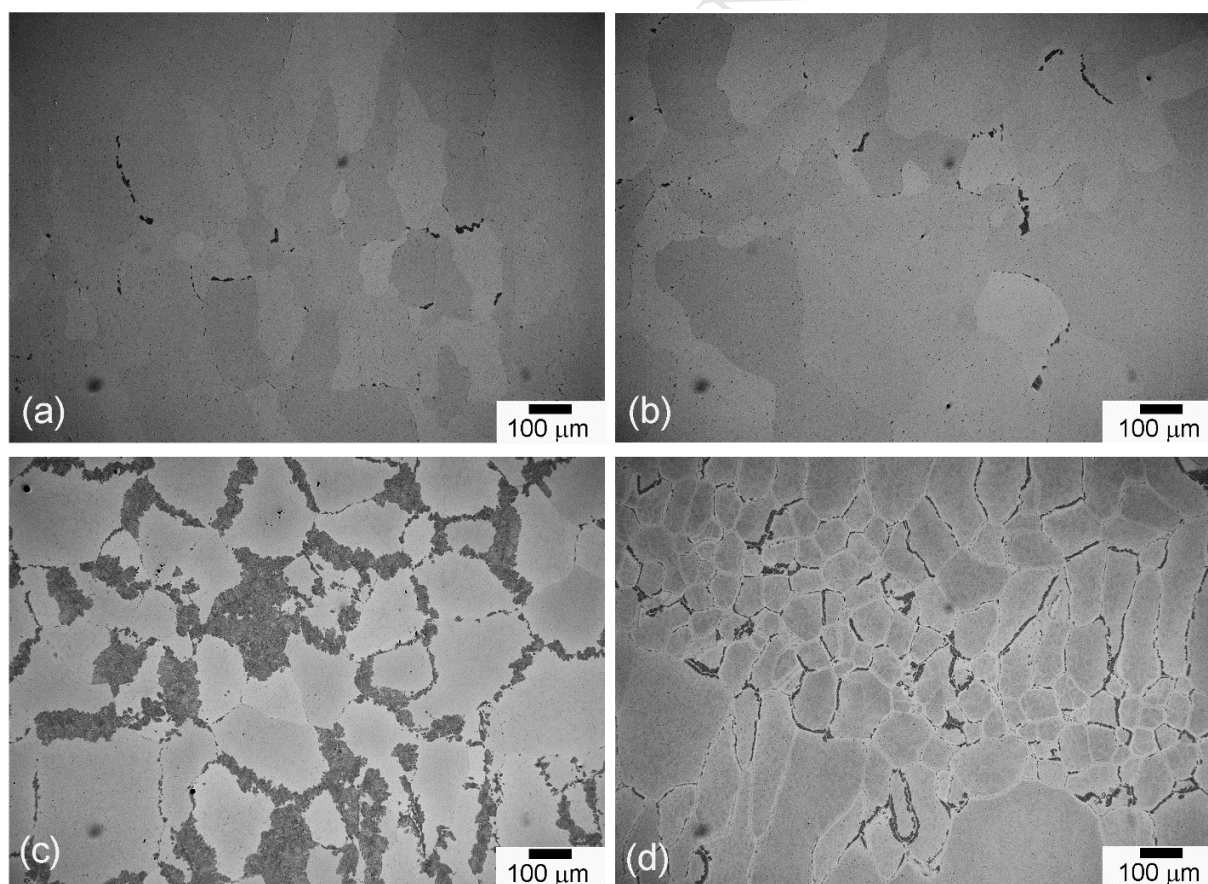


Fig. 11. Microstructure after the homogenized alloys were aged at 500 °C for 20 h: (a) U10Mo, (b) U9.8Mo0.2Cr, (c) U9.8Mo0.2Ni, (d) U9.8Mo0.2Co.

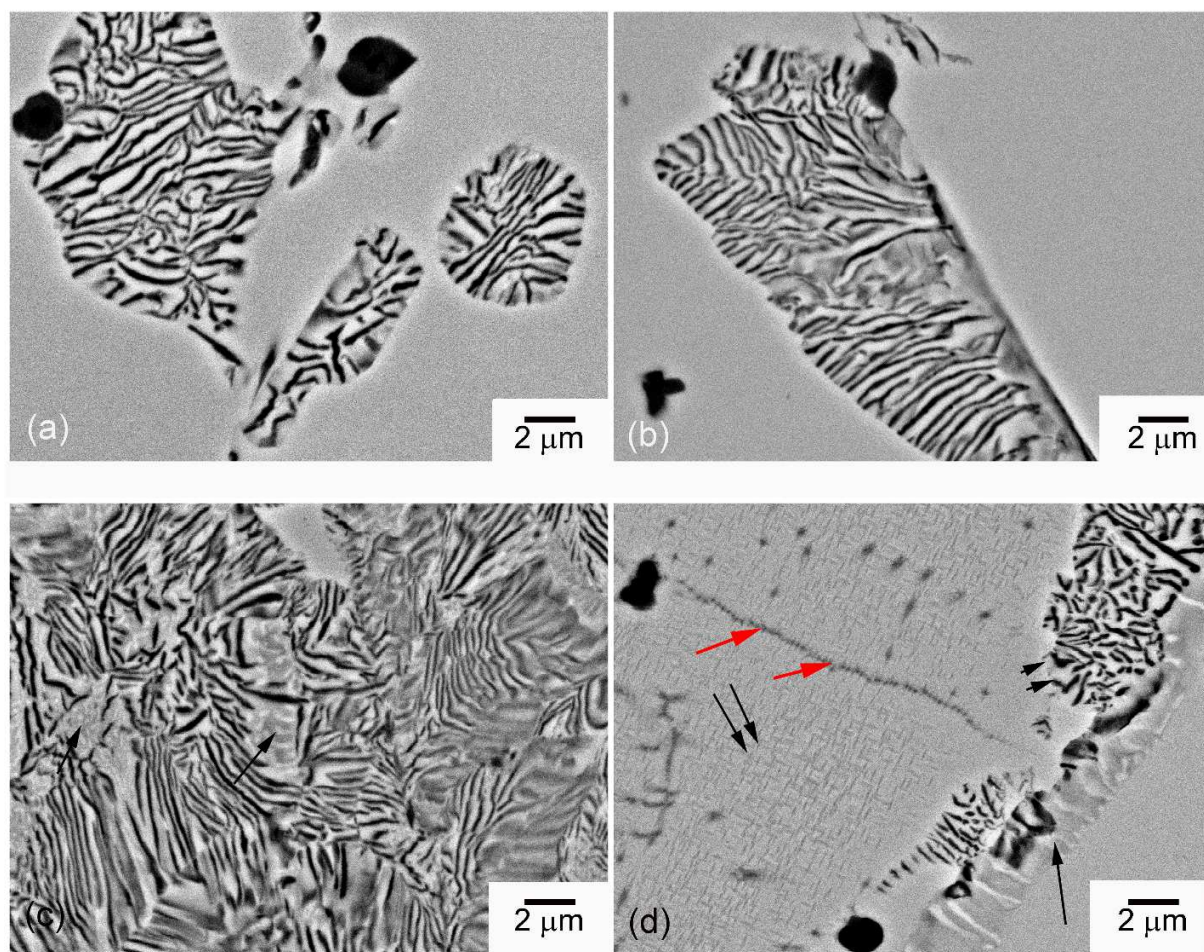
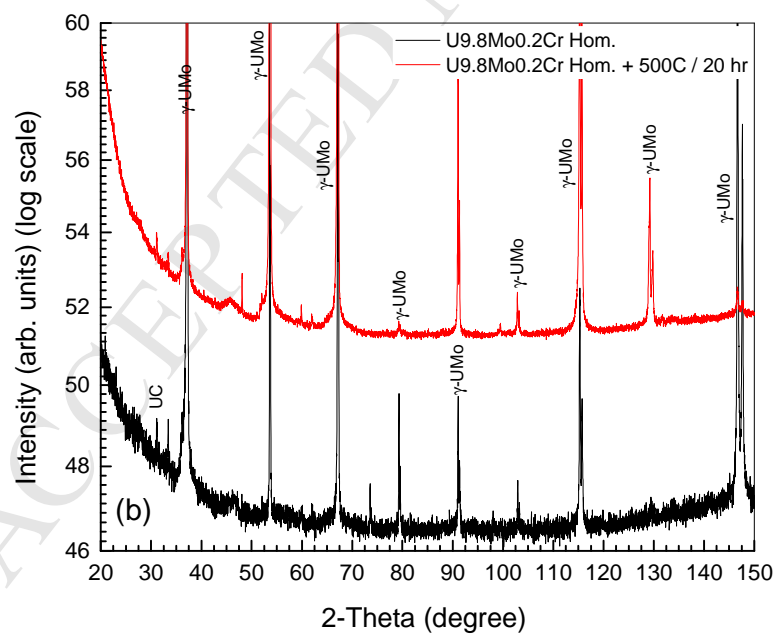
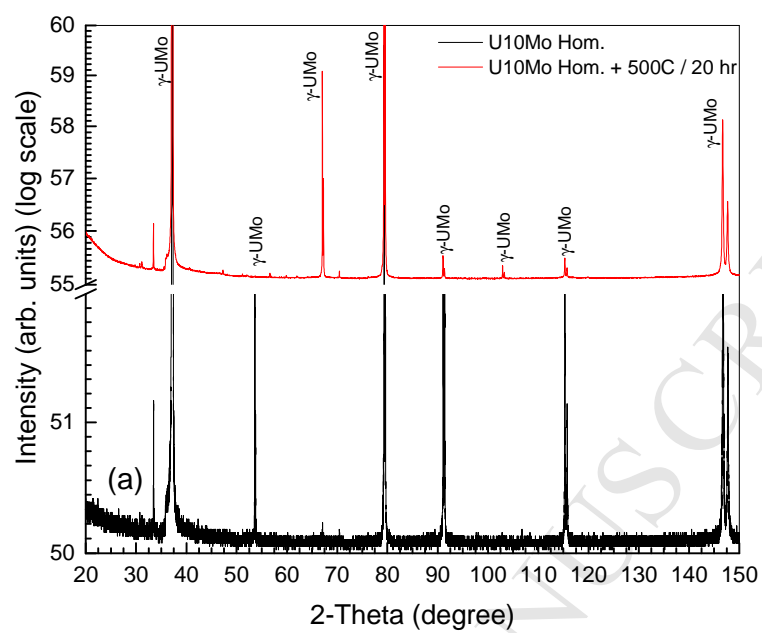


Fig. 12. Higher magnification images showing the microstructural details observed in the homogenized alloys after 500 °C/20 h exposure: (a) U10Mo shows the typical DP-based eutectoid transformation; (b) U9.8Mo0.2Cr shows DP-type eutectoid transformation products that are very similar to that in U10Mo; (c) U9.8Mo0.2Ni shows significant DP-type transformation; arrow shows bright-contrast lamellar structure formation within regular DP colony; (d) U9.8Mo0.2Co shows two types of lamellar structure forming along grain boundary; the single long, black arrow represents the U6Co type-lamellar structure that forms during homogenization, the short, black double arrow shows the regular DP-based eutectoid transformation products, the long, black double arrow shows uniform precipitation with interpenetrant morphology within the γ -UMo grain interior, and the long, red arrow shows network-like precipitation within the γ -UMo grain interior.



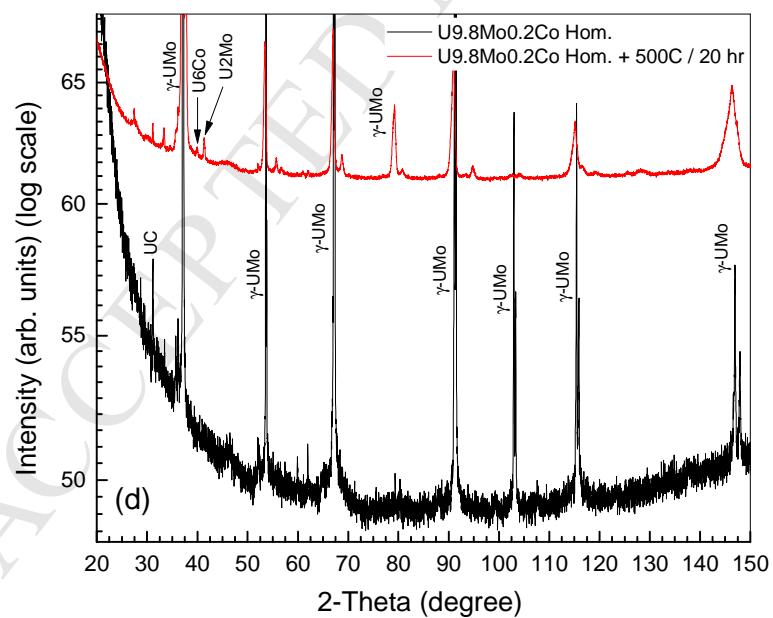
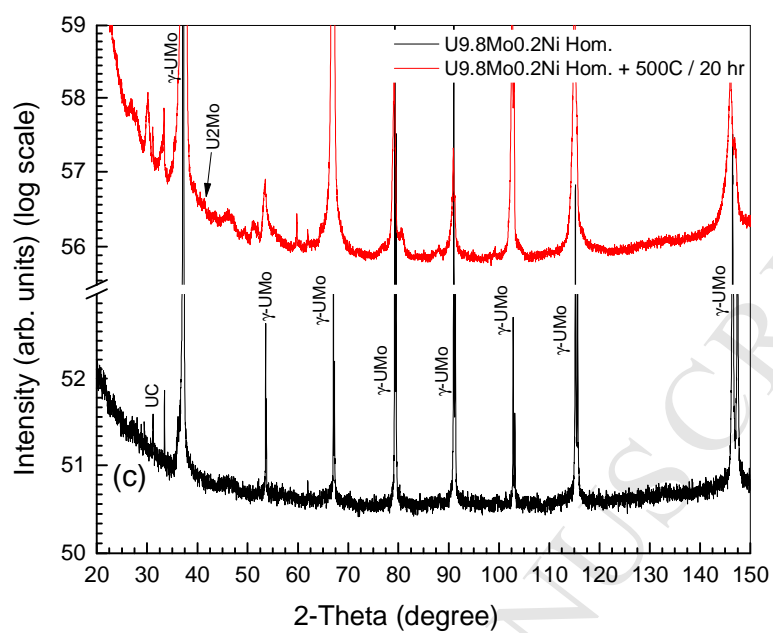


Fig. 13. XRD profiles of (a) U10Mo, (b) U9.8Mo0.2Cr, (c) U9.8Mo0.2Ni, (d) U9.8Mo0.2Co.